Research Article

Yuan-Chang Liang* and Chia-Hung Huang

Microstructure-dependent photoelectrocatalytic activity of heterogeneous ZnO–ZnS nanosheets

https://doi.org/10.1515/ntrev-2022-0076
received November 10, 2021; accepted February 17, 2022

Abstract: ZnS crystallite-loaded ZnO sheet composites were successfully synthesized through vulcanization of hydrothermally derived porous ZnO sheet templates. The sulfur precursor (Na_2S: 0.05–0.25 M) concentration affects the ZnS loading content and surface morphology of the ZnO–ZnS composites. A higher sulfur precursor concentration increased the ZnS loading content and decreased the porosity of the ZnO–ZnS composites. The ZnO–ZnS sheet composites with the atomic composition ratio of ZnO larger than that of the decorated ZnS exhibited an enhanced photoactivity. By contrast, the overloading of ZnS crystallites on the ZnO template decreased photoactivity. The ZnO–ZnS sheet composite with a S/O atomic ratio of 0.61 exhibits the highest photoactivity among various samples. The enhanced charge separation efficiency because of the formation of ZnO/ZnS heterojunctions and porous structure allowed the synthesis of the ZnO–ZnS composite *via* hydrothermal vulcanization with 0.05 M Na_2S, and shows the higher photoelectrochemical (PEC) degradation ability towards Rhodamine B solution among various samples. The scavenger tests and the proposed PEC-degradation mechanism demonstrate that superoxide radicals are the main active species for the degradation of the RhB solution. The experimental results herein show that the porous ZnO–ZnS sheet composite with a suitable phase ratio is promising for photoelectrocatalyst applications.

Keywords: sheet composite, microstructure, photoactive performance

1 Introduction

ZnO is widely used for degrading organic pollutants due to its variety of preparation methods, low cost, nontoxicity, and strong redox ability [1,2]. Several routes have been established for the synthesis of low-dimensional ZnO crystals with various morphologies, such as hydrothermal method, chemical bath deposition, vapor deposition, and sputtering deposition [3–6]. It has been shown that the advantages of a high specific surface area, abundant surface active sites, and strong adsorption capacity make low-dimensional ZnO nanomaterials suitable for catalytic reaction applications. Recently, the development of porous ZnO nanostructures shows that the tiny pores in ZnO substantially improve their specific surface area size, light absorption ability, and surface active site number in comparison with the ZnO with solid crystal characteristics [3,7]. Therefore, porous ZnO nanomaterials are a good candidate for use in photoactive devices with high performance. Furthermore, ZnS because of its remarkable chemical stability against oxidation and hydrolysis also receives much attention for application in photoactive devices [8]. Great efforts have been steadily devoted to synthesize ZnS nanostructures, aiming to enhance their photoactive performance *via* controlling their specific surface area and photoinduced charge separation efficiency. Several approaches have been adopted for synthesizing ZnS nanostructures with different morphologies for high-performance applications in photoactive devices [9,10].

Photocatalytic activation of semiconductors is mainly dominated by the number of excitons under irradiation to generate free radicals to degrade target pollutants [11–17]. Therefore, the control of photoinduced charge separation efficiency is a key for ZnO or ZnS to perform high photocatalytic performance. Several approaches including the incorporation of impurity, crystal defect, and formation of a heterostructure have been widely adopted for ZnO or ZnS for improved photoactive performance [18–20]. Among these approaches, the formation of ZnO- or ZnS-based heterostructures with a suitable band alignment

* **Corresponding author: Yuan-Chang Liang,** Department of Optoelectronics and Materials Technology, National Taiwan Ocean University, Keelung 20224, Taiwan, e-mail: yuanvictory@gmail.com
Chia-Hung Huang: Department of Optoelectronics and Materials Technology, National Taiwan Ocean University, Keelung 20224, Taiwan

between the constituent compounds is of potential importance to enhance the photoactive performance of ZnO or ZnS. This is due to various choices of coupling semiconductors to be integrated into the ZnO or ZnS, and the formation of a heterostructure has a high degree of freedom to manipulate the photoactive performance of the semiconductors. More importantly, due to the suitable Type II band alignment between the ZnO and ZnS, the construction of the ZnO/ZnS heterostructure has been shown to be a promising combination to improve the photoactive performance of the constituent counterparts [21].

The morphology, microstructure, composition ratio, and band alignment are factors that affect the final photoactive performance of the ZnO–ZnS heterostructures [22,23]. The control of ZnO–ZnS heterostructures with abundant active surfaces and interfaces for the photocatalytic process and design of the heterojunction to promote the separation and transfer of photogenerated electrons and holes with suitable bandgap positions are still a challenge to synthesize ZnO–ZnS composites with high photoactive performance. In this study, porous ZnO–ZnS sheet-like nanostructures are synthesized using a hydrothermal vulcanization method with porous ZnO sheet templates. The porous ZnO sheet templates can improve photocatalytic activity due to their high specific surface area. Moreover, the formation of ZnO–ZnS porous nanosheets by varying the parameters of hydrothermal vulcanization utilizes the control of microstructures of the ZnO–ZnS sheet composites to obtain high photoactive performance at a low-temperature and low-cost process. The systematic investigation on the vulcanization process-dependent microstructure evolution of ZnO–ZnS sheet composites in this study provides a promising approach to synthesize and design ZnO–ZnS sheet composites for photoelectrocatalytic device applications with high efficiency.

2 Experiments

2.1 Preparation of porous ZnO nanosheet templates

The ZnO nanosheets were grown on an F-doped tin oxide (FTO) glass substrate by the hydrothermal approach. A 100 mL aqueous solution consisting of zinc nitrate hexahydrate ($Zn(NO_3)_2{\cdot}6H_2O$; 4.477 g) and urea ($(NH_2)_2CO$; 16.67 g) dissolved in it was used as a precursor solution. The hydrothermal reaction was performed at 90°C for 4 h in this study. After the hydrothermal deposition, template products identified as $Zn_4CO_3(OH)_6{\cdot}H_2O$ nanosheets were formed. The template nanosheet products were further annealed at 400°C for 30 min in ambient air to form a crystalline porous ZnO nanosheet template.

2.2 Preparation of ZnO–ZnS heterostructures

ZnO–ZnS heterostructures were prepared by the hydrothermal vulcanization method. The ZnO nanosheet templates were immersed in 0.05, 0.1, and 0.25 M $Na_2S{\cdot}9H_2O$ dissolved solutions, respectively. The samples for the ZnO template treated with 0.05, 0.1, and 0.25 M $Na_2S{\cdot}9H_2O$ are named ZS-1, ZS-2, and ZS-3, respectively. The hydrothermal reaction was performed at 70°C for 2 h. For band energy evaluation, the pure ZnS nanosheets were further made using 0.5 M $Na_2S{\cdot}9H_2O$ solution for hydrothermal vulcanization of the ZnO nanosheet template. The final products were washed with deionized water and dried at 60°C in a drying oven for 24 h.

2.3 Material analysis and characterization tests

The crystallographic structures of the products were characterized by X-ray diffraction (XRD) using a Bruker D2 PHASER. The morphologies of the products were investigated using field emission scanning electron microscopy (FE-SEM; JEOL JSM-7900F). High-resolution lattice images, composition, and selected area electron diffraction of the products were recorded using high-resolution transmission electron microscopy (HR-TEM; JEOL JEM-2100F) equipped with an energy-dispersive X-ray spectroscope (EDS). X-ray photoelectron spectroscopy (XPS; PHI 5000 VersaProbe) was used to analyze the elemental binding energies of the products. The analysis of absorbance spectra of the products was conducted using a UV-Vis spectrophotometer (Jasco V750).

The photoelectrochemical (PEC) and impedance spectroscopy properties of the products were characterized in a three-electrode electrochemical quartz cell using an electrochemical analyzer (SP-150, BioLogic). The as-synthesized product was used as the working electrode as well as a Pt wire and an Ag/AgCl electrode were used as the counter electrode and reference electrode,

respectively. The electrolyte is a 0.5 M Na_2SO_4 solution and the irradiation source for measurements is excited with a 100 W Xe arc lamp. The light intensity on the sample is approximately 3.12 mW/cm^2. The photoelectrocatalytic activities of the products were evaluated by PEC-degrading rhodamine B (RhB) solution with different irradiation durations of 15, 30, 45, and 60 min. Moreover, the dark balance absorption tests of various samples for 30 min are also conducted. A total of 10 mL of RhB solution (10^{-5}) M was added to 10 mL of 0.5 M Na_2SO_4 solution to form a homogeneous aqueous solution for PEC-degradation system use, and the applied potential was varied from 0 to 1 V during PEC-degradation tests. The concentration of the degraded RhB solution was evaluated by recording the absorbance spectra intensity variation ratio of the RhB solution before and after the test. The C_t/C_0 is evaluated from I_t/I_0, in which C_0 is the initial concentration of the RhB solution, C_t is the concentration of that at a different interval during the degradation process, I_0 is the absorbance spectrum intensity of the initial RhB solution, and I_t is the absorbance spectrum intensity of the RhB solution at a different interval during the degradation process.

3 Results and discussion

Figure 1(a) shows the porous ZnO nanosheet template. The sheet thickness is approximately 20 nm. Moreover, numerous tiny nanoscaled pores existed in the sheet. Figure 1(b) and (c) display the morphology of the porous ZnO nanosheet template treated with different vulcanization processes with various sulfur precursor concentrations of 0.05 M, 0.1 M, and 0.25 M Na_2S. Figure 1(b) and (c) indicate that the morphology of the ZnO nanosheet template did not show a marked change after the vulcanization process with the lower sulfur concentration below 0.1 M. The sheet template still maintained a porous structure with abundant tiny pores on it. Notably, when the sulfur precursor concentration was substantially increased to 0.25 M, the morphology changed to be more solid, and no distinct porous structure was observed for the ZnO sheet template after vulcanization. The addition of Na_2S into the hydrothermal reaction solution results in the ion exchange between S^{2-} from the dissolved Na_2S and O^{2-} from the ZnO template, and this ion exchange process promotes the formation of ZnS crystallites on the surfaces of the ZnO sheet template [24–26]. The inward diffusion of

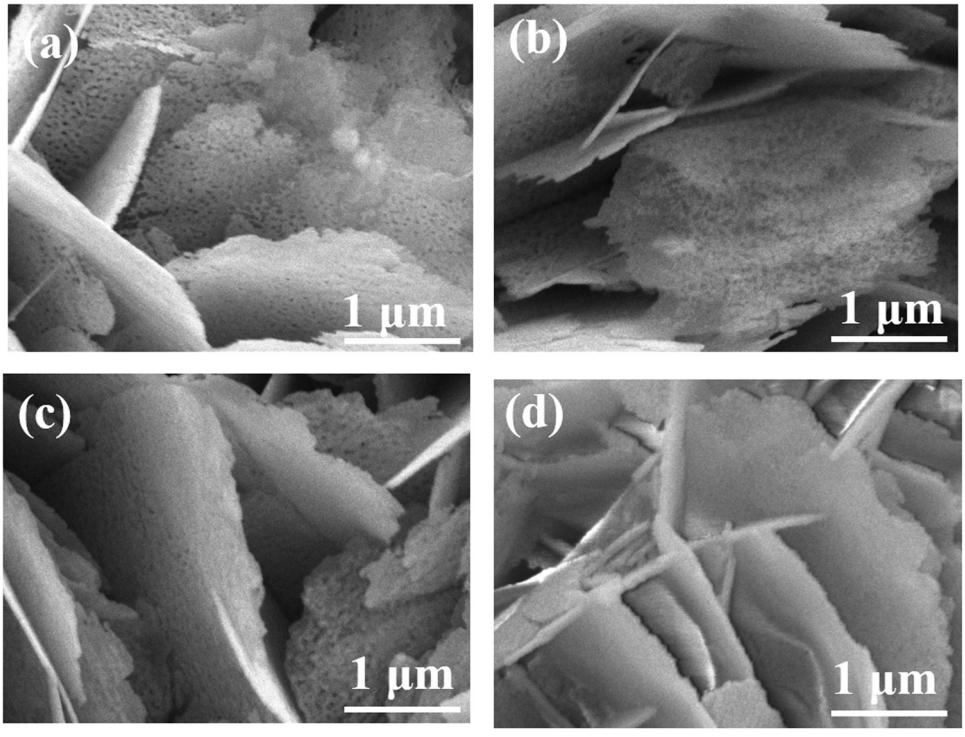

Figure 1: SEM images of various products: (a) ZnO template, (b) ZS-1, (c) ZS-2, and (d) ZS-3.

S^{2-} to interact with Zn^{2+} in the ZnO template forms the ZnS phase during the hydrothermal vulcanization process. Notably, even the vulcanization process was conducted for the ZnO sheet template with an increased sulfur precursor concentration ranging from 0.01 to 0.25 M, the sheet-like feature of the ZnO template was still maintained in this study, revealing a gradual dissolve of the ZnO phase and the formation of ZnS phase reached an equilibrium state during the current hydrothermal vulcanization processes. With the increase of the sulfur ion source, more ZnO might convert into ZnS with an increased reaction degree of ion exchange, and the generated ZnS crystallites will cover the residual ZnO surface and reorganize the surface topography of the porous ZnO sheet template. Therefore, the porous ZnO sheet template treated with the highest sulfur concentration herein causes more ZnS crystallites to form, leading to the disappearance of the porous surface of the ZnO sheet template.

Figure 2 shows the XRD patterns of the ZnO sheet template treated with and without various vulcanization processes. In Figure 2(a), in addition to FTO Bragg reflections, the distinct and intense Bragg reflections centered at 31.77°, 34.42°, 36.25°, 47.54°, and 56.6° are characteristics to wurtzite ZnO (100), (002), (101), (102), and (110) planes according to JCPDS No. 36-1451. The substantially intense nonpolar crystallographic planes of (100) and (101) and weak intensity of the *c*-axis crystal plane (002) reveal the sheet morphological feature of the ZnO herein [3,27]. When the ZnO sheet template was treated with the vulcanization process, additional new Bragg reflections centered at 28.56°, 47.51°, and 56.29° are observed and ascribed to the cubic ZnS (111), (220), and (311) crystal planes according to JCPDS No. 05-0566 in Figure 2(b)–(d). Notably, the ZnO(102) and (110) positions are close to those of the ZnS (220) and (311), respectively. However, the markedly decreased intensity and broadened peak width of the Bragg reflections centered at approximately 47.51–47.54° and 56.29–56.6° might reveal the overlap of the Bragg reflections of the ZnO and ZnS phase planes in these two theta angle regions. The XRD results reveal that the vulcanization processes herein are effective to induce the partial ZnO template crystal to transfer into the ZnS phase. Furthermore, the intensity of the characteristic crystallographic plane of cubic ZnS (111) was substantially increased with the increased sulfur precursor concentration, revealing an

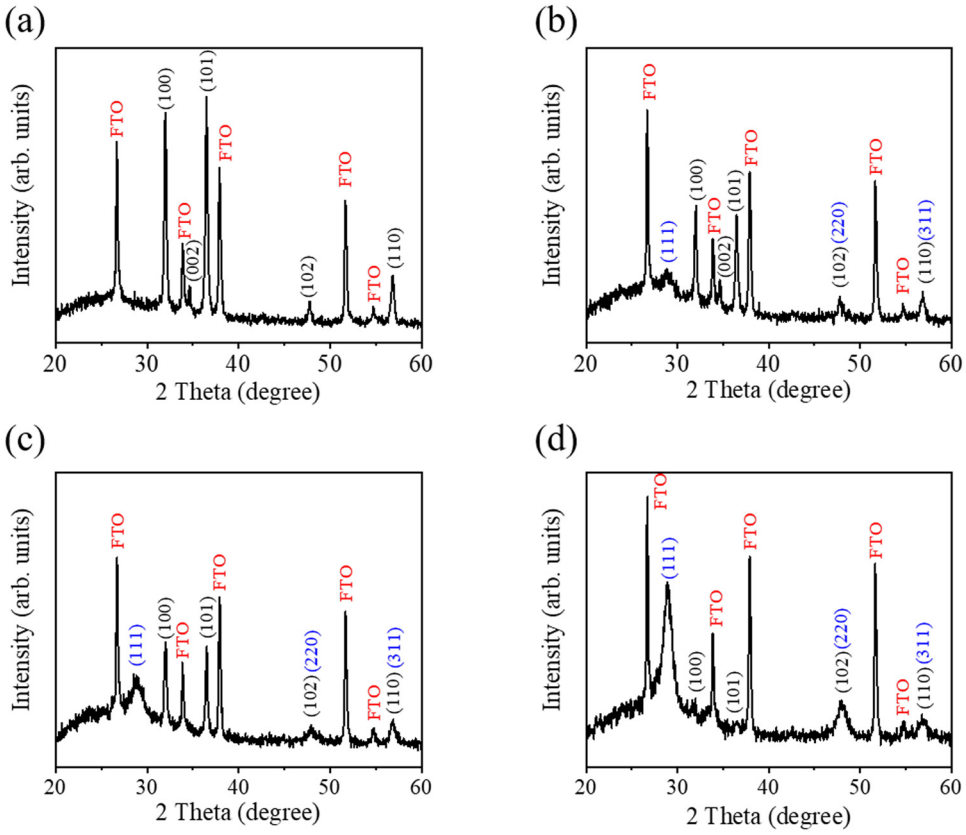

Figure 2: XRD patterns of various products: (a) ZnO template, (b) ZS-1, (c) ZS-2, and (d) ZS-3. The ZnO and ZnS crystallographic planes are marked with black and blue, respectively.

increased content of ZnS crystals in the sample [21,26]. From the comparison and investigation of the main characteristic crystallographic planes (100) and (101) of the ZnO sheet and (111) of ZnS crystals, the ZS-1, ZS-2, and ZS-3 show the clear coexistence of ZnO and ZnS phases in the products and are in a crystalline composite structure. Notably, the substantially weak Bragg reflections of ZnO(100) and (101) together with a markedly intense Bragg reflection of ZnS (111) in Figure 2(d) demonstrates that the ZnO template has been massively vulcanized for the ZS-3.

Figure 3(a) shows the low-magnification TEM image of the ZS-1 nanosheet. Visible pores in a nanometer scale existed in the sheet structure, and the diameter of the sheet is approximately 1 μm. The HRTEM images taken from the outer and inner pore regions of the sheet are displayed in Figure 3(b)–(e). The visible lattice fringes arranged with an interval of 0.31 nm corresponded well to the interplanar spacing of the (111) plane of the cubic ZnS structure. Moreover, some inner regions of the HR images displayed twisted and overlapped lattice fringes that might be associated with the overlapped crystals of ZnO and ZnS. Figure 3(f) demonstrates the selected-area electron diffraction (SAED) pattern of the ZS-1 nanosheet. The SAED pattern revealed a multiringed, multiphase pattern with ZnO (002), (102), (200) and ZnS (111), (311). The SAED pattern presents the coexistence of ZnO and ZnS in the ZS-1 nanosheet and the result is consistent with the aforementioned XRD pattern. The EDS spectra in Figure 3(g) clarify the elemental composition of the ZS-1 nanosheet. In addition to Cu and C signals from the TEM grid, no impurity elements are detected herein. The atomic percentages of Zn, O, and S for the ZS-1 nanosheet is 48, 32.2, and 19.8, respectively. Furthermore, the spatial elemental distribution of Zn, S, and O in the ZS-1 sheet structure is shown in Figure 3(h). The elemental distribution of Zn, O, and S atoms over the selected nanosheet reveals that the ZS-1 has a homogeneous composition of ZnO and ZnS that coexisted in the nanosheet.

Similarly, the ZS-2 nanosheet also presents a porous sheet structure in Figure 4(a). The existence of lattice fringes of ZnS (111) is also demonstrated in the outer regions of the selected HR images in Figure 4(b) and (c). Moreover, overlapped and twisted lattice fringes characterized by the coexistence of the ZnO and ZnS phases are presented in HR images. The EDS spectra in Figure 4(d) reveal that the atomic percentages of Zn, O, and S are approximately 57.5, 23.0, and 19.5, respectively for the ZS-2 nanosheet.

Figure 5(a) represents the low-magnification TEM image of the ZS-3 nanosheet. The ZS-3 nanosheet has a different surface feature from those of ZS-1 and ZS-2. The ZS-3 nanosheet has a dense and particle aggregated surface feature. No pores are visibly distinguished in the ZS-3. From Figure 5(b) and (c), the HRTEM micrograph indicated clear ZnS (111) lattice fringes. The grayscale comparison in these HR images presents clear particle aggregated features at the peripheral region of the

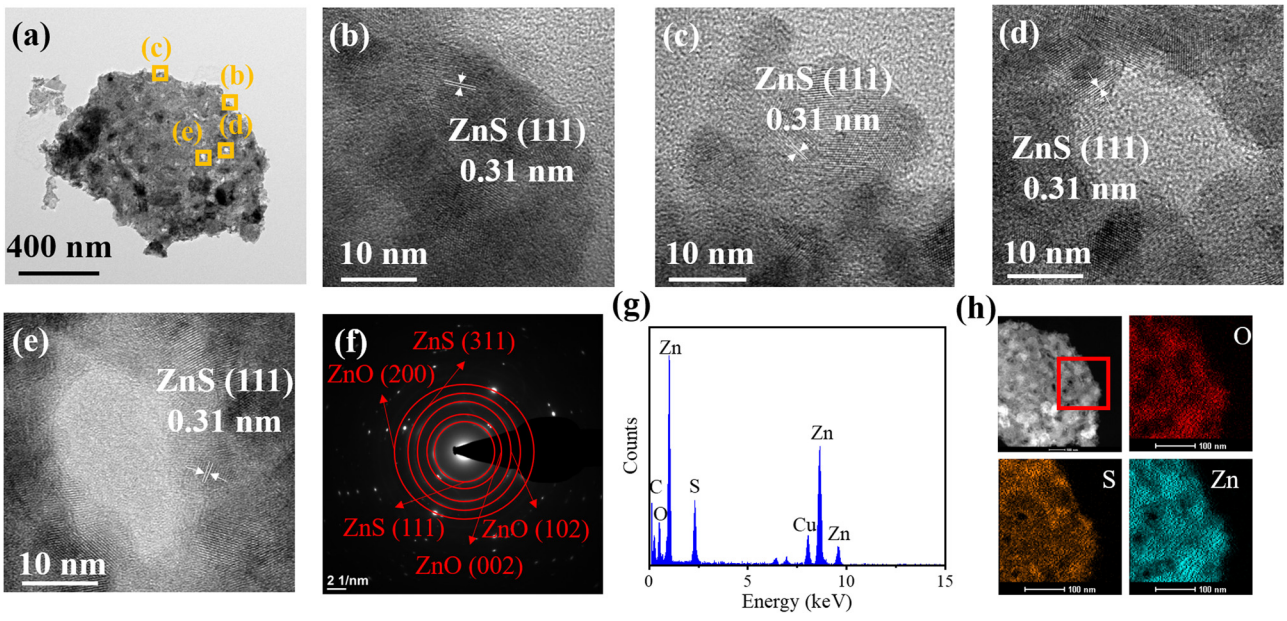

Figure 3: TEM analysis of the ZS-1: (a) low-magnification image. (b)–(e) HRTEM images of various local regions in image (a). (f) SAED pattern. (g) EDS spectrum. (h) Elemental mapping images.

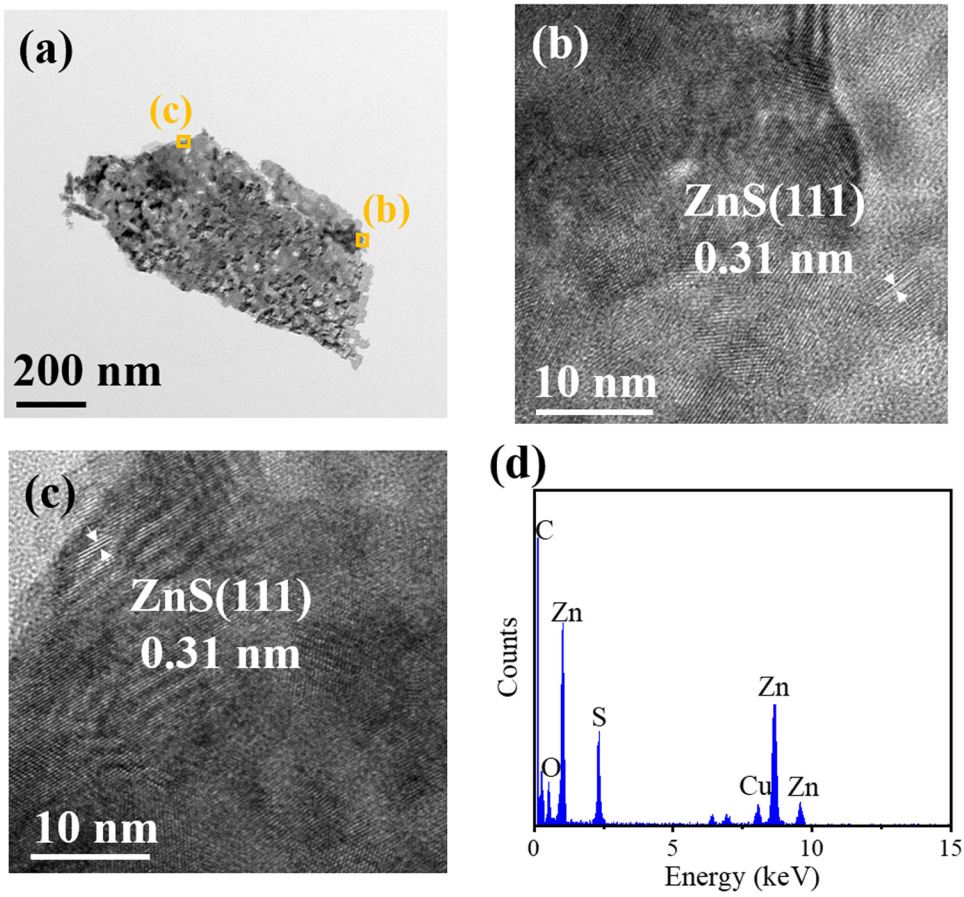

Figure 4: TEM analysis of the ZS-2: (a) low-magnification image. (b) and (c) HRTEM images of various local regions in image (a). (d) EDS spectrum.

nanosheet. This might be associated with an increased crystalline quality of ZnS crystallites at the given vulcanization process [26]. The SAED pattern in Figure 5(d) shows ZnO (002) and (103), ZnS (111), (220), and (103) planes, revealing that the ZS-3 consisted of ZnO and ZnS phases. From the EDS spectra of the ZS-3 (Figure 5(e)) the Zn, O, and S atomic percentages of the ZS-3 are found to be 62.0, 8.2, and 29.8%, respectively. Notably, the summarized compositions comparison of the S/O atomic ratio from TEM-EDS spectra for ZS-1, ZS-2, and ZS-3 are 0.61, 0.85, and 3.63, respectively, highlighting that more ZnO crystals were converted into the ZnS phase with an increased sulfur precursor concentration during the vulcanization process.

The narrow scan XPS spectra of Zn2p regions for the ZS-1, ZS-2, and ZS-3 are presented in Figure 6(a)–(c), respectively. The $Zn2p_{3/2}$ and $Zn2p_{1/2}$ peaks are centered at approximately 1021.1 and 1044.1 eV, respectively. The spin–orbit splitting of approximately 23 eV between the $Zn2p_{3/2}$ and $Zn2p_{1/2}$ core–level components reveals the Zn^{2+} state nature herein [21,28]. Notably, the core–level Zn2p binding energies of Zn–O are close to those of Zn–S [21]. Due to the similar Zn^{2+} binding energy of ZnO and ZnS phases, there are no substantial differences in the obtained Zn2p spectra among various samples. Figure 6(d)–(f) presents XPS S2p spectra of various samples. Notably, asymmetric S2p spectra can be further deconvoluted into two subpeaks that are centered at approximately 161.1 and 162.1 eV and are attributed to $S2p_{3/2}$ and $S2p_{1/2}$ of S^{2-} binding states, respectively [21,25]. Moreover, the peak intensity ratio of $S2p_{1/2}$ to $S2p_{3/2}$ was approximately 1:2, revealing that the ZnS phase has been successfully synthesized by O^{2-} and S^{2-} ion exchange during the given vulcanization processes for the ZnO sheet template. Moreover, the higher S2p spectrum intensity of ZS-3 reveals higher content of the ZnS phase in the ZS-3 composite. The O1s XPS spectra of ZS-1, ZS-2, and ZS-3 are shown in Figure 6(g)–(i), respectively. The decreased O1s spectrum intensity for the composite structure with an increased sulfur precursor concentration demonstrates an increased sulfidation degree of the ZnO template to form more Zn–S bonds [29]. The O1s

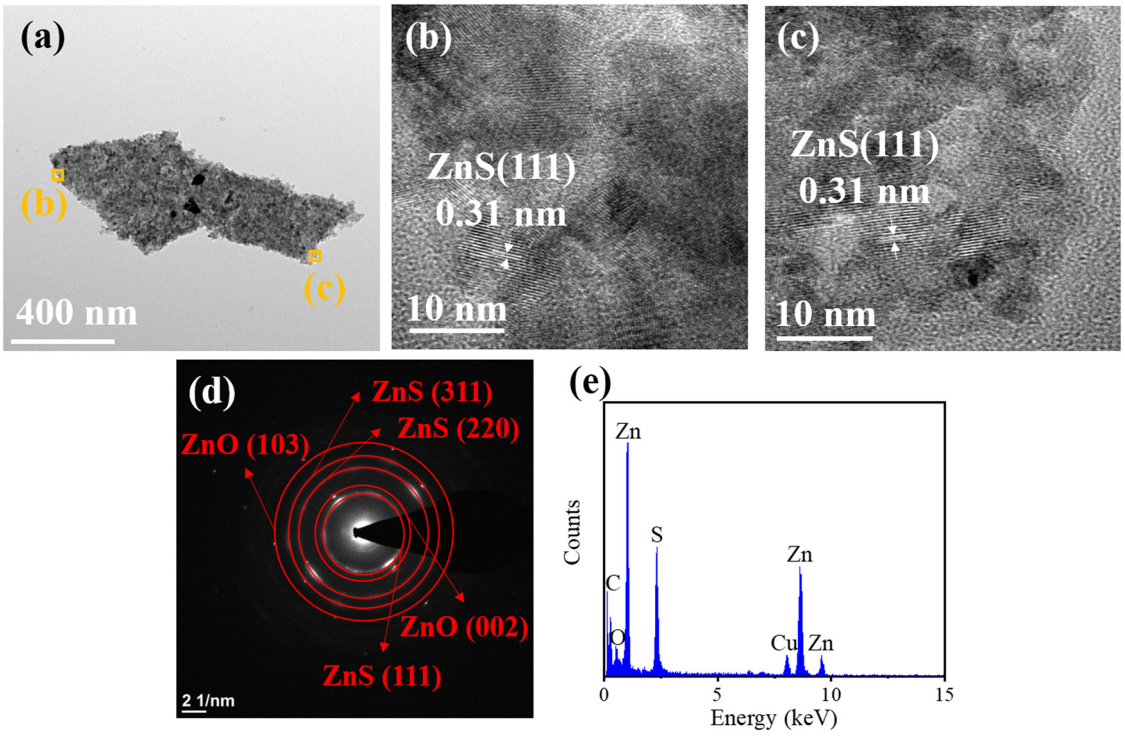

Figure 5: TEM analysis of the ZS-3: (a) low-magnification image. (b) and (c) HRTEM images of various local regions in image (a). (d) SAED pattern. (e) EDS spectrum.

spectra are further split into two subpeaks. The subpeak centered at approximately 530.7 eV (blue line) is assigned to the crystal lattice oxygen ions in ZnO, and the peak centered at approximately 531.5 eV (green line) is associated with the oxygen vacancy and/or absorbed OH^- in the ZnO lattice [30]. The XPS results herein reveal that a composite structure of ZnO–ZnS was formed for the ZS-1, ZS-2, and ZS-3 samples.

The optical absorption spectra of various samples are shown in Figure 7(a). It can be clearly seen that the ZnO template has a strong absorption edge at approximately 380 nm. The optical absorption edge gradually shifted to a shorter wavelength for the ZnO template treated by vulcanization processes with an increased sulfur precursor concentration. Notably, dual optical absorption edges are visibly observed for the ZS-1, ZS-2, and ZS-3. The dual absorption edges are associated with the contribution of two constituent phases of ZnO and ZnS, and this has also been demonstrated in the ZnO–ZnS heterostructure synthesized *via* a solid-state low-temperature synthesis method [31]. Moreover, from Figure 7(a), all the prepared products have optical absorption edges located in the UV range, revealing they are UV-light sensitizer materials. The band gap energy (E_g) of the products can be further calculated according to the equation $(\alpha h\nu)^2 = A(h\nu - E_g)$, where A is a constant, E_g is the band gap energy, h is the Planck constant, and α is the absorption coefficient. Figure 7(b) and (c) illustrate the $(\alpha h\nu)^2$ *versus* photon energy plots used for the evaluation of the band gap energy of the constituent semiconductors. The band gap energy was estimated to be approximately 3.2 eV for ZnO [27] and 3.4 eV for ZnS herein. The evaluated ZnS band gap energy is close to the reported value of ZnS nanoparticles synthesized *via* wet chemical methods [32]. Moreover, Figure 7(c) reveals the coexistence of the band gap energies of ZnO and ZnS phases; this is in agreement with the previous structural analysis of ZS-3 associated with the formation of the ZnO–ZnS composite structure.

The cycling photocurrent density *versus* time (I–t) curves under chopping irradiation for ZnO, ZS-1, ZS-2, and ZS-3 are shown in Figure 8(a). The average photocurrent densities of ZnO, ZS-1, ZS-2, and ZS-3 photoelectrodes are approximately 0.61, 1.22, 1.06, and 0.23 mA/cm^2 at 0.5 V *vs* Ag/AgCl. The ZS-1 shows the highest photocurrent density at the test cycles. Moreover, both the ZS-1 and ZS-2 exhibit a higher photoresponse than that of the ZnO template, implying improved charge separation and transfer abilities in the ZS-1 and ZS-2. By contrast, the ZS-3 demonstrates the deteriorated photoresponse performance in comparison with that of the pristine ZnO. The result reveals that the content of ZnS

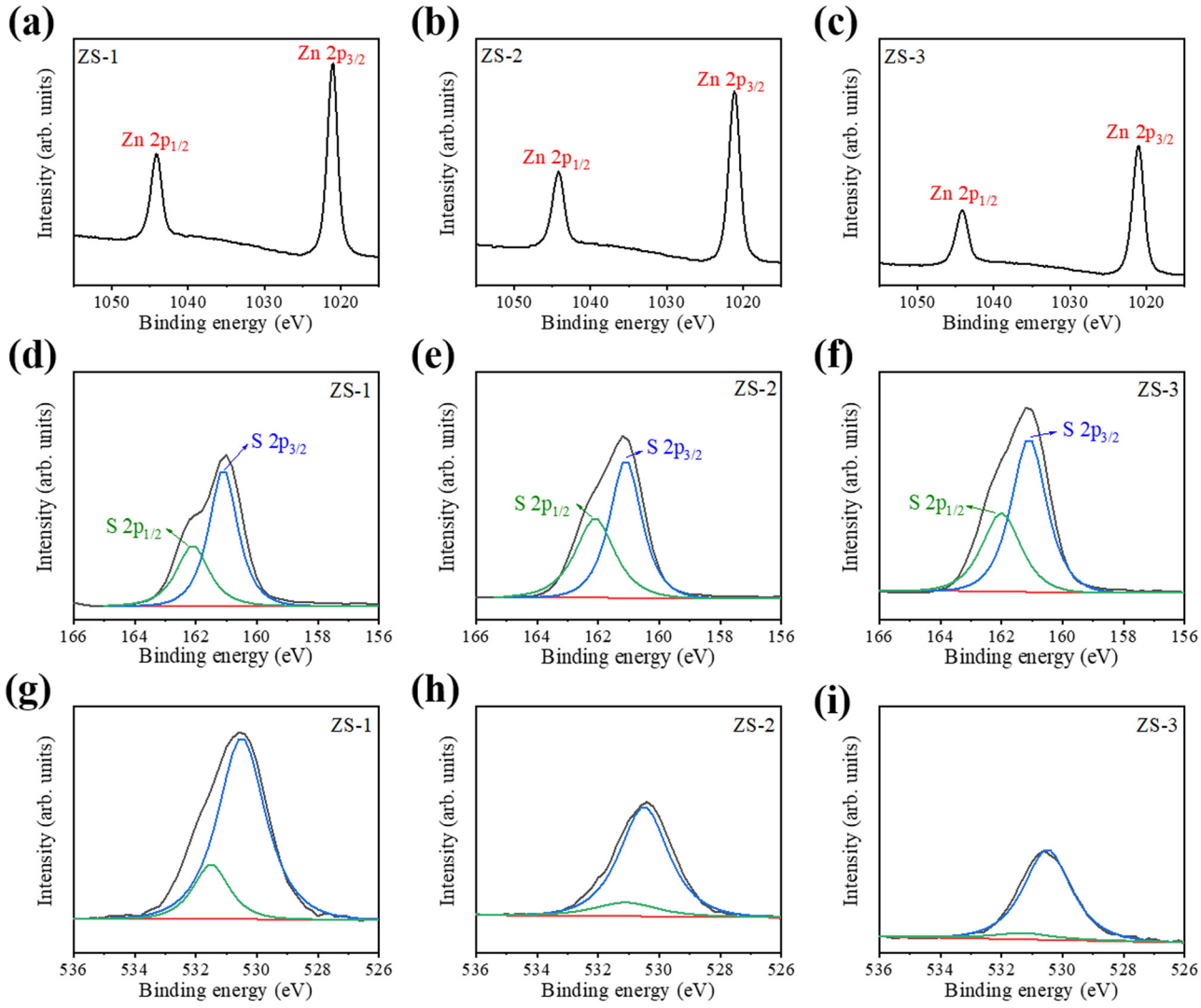

Figure 6: High-resolution XPS spectra in Zn2p: (a) ZS-1, (b) ZS-2, and (c) ZS-3. High-resolution XPS spectra in S2p: (d) ZS-1, (e) ZS-2, and (f) ZS-3. High-resolution XPS spectra in O1s: (g) ZS-1, (h) ZS-2, and (i) ZS-3.

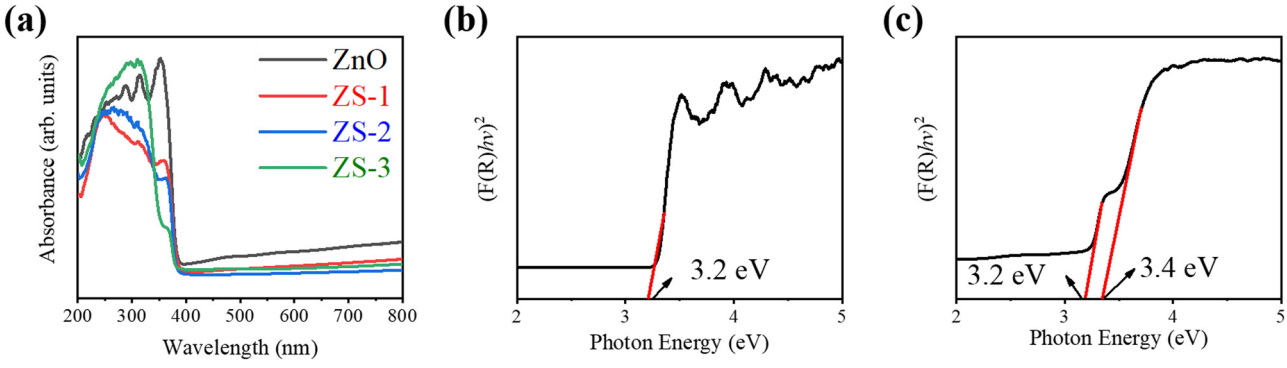

Figure 7: (a) UV-Vis absorption spectra of various products. (b) The band gap evaluation of the ZnO template. (c) The band gap evaluation of ZS-3.

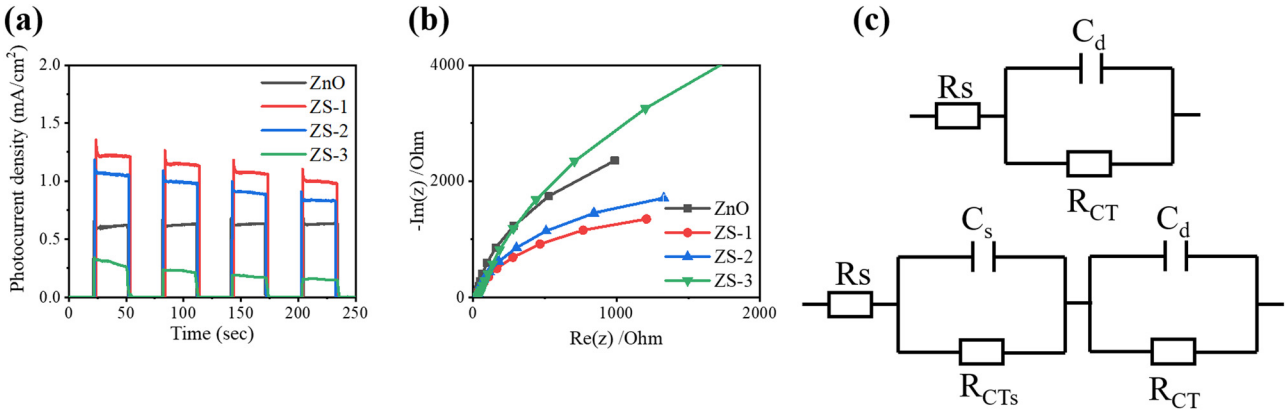

Figure 8: (a) Chronoamperometric *I–t* curves collected at 0.5 V *vs* Ag/AgCl for various products under chopping irradiation. (b) Nyquist plots of various products under irradiation. (c) The possible equivalent circuits employed to fit the Nyquist plots of various products. The upper one is for the ZnO template, and the lower one is for the ZnO–ZnS composites.

in the ZnO–ZnS composite affects the photo-induced charge separation efficiency in the composite structure. The fewer ZnS crystallites in the porous ZnO–ZnS sheet-like composite structure improves the separation of electron–hole pairs between ZnO and ZnS under irradiation, and thus, have a better photoresponse. By contrast, the photo-induced electron–hole pairs are unable to be separated effectively for massive ZnS crystallites in the solid ZnO–ZnS sheet-like composite structure. It has been shown that the thick ZnS shell layer in the ZnO–ZnS core–shell nanofibers suppresses the tunneling efficiency of the holes from the ZnO core to the ZnS shell [29], and this work supports the observed deteriorated photoresponse performance of the ZS-3 herein. Notably, the photocorrosion phenomenon was observed from the ZS-1 and ZS-2 composites. The photocorrosion causes the slightly decreased photocurrent with the irradiation on/off cyclic number, and this phenomenon might be associated with the accumulation of excessive light-induced holes on the ZnS surface at the given test condition [33]. Figure 8(b) shows the Nyquist plots of various products. Comparatively, the ZS-1 displays the smallest semicircle radius among various products. The smaller radius of the Nyquist plot's semicircle implies lower interfacial charge transfer resistance in semiconductor heterostructures [34–36]. The corresponding equivalent circuits for the pristine ZnO template and ZnO–ZnS composite are shown in Figure 8(c). Notably, R_s represents the series resistance of the electrochemical device. C_s and R_{CTs} represent the capacitance phase element and charge transfer resistance of the depletion layer of the semiconductor, respectively. C_d and R_{CT} are the capacitance phase element and the charge transfer resistance at the double layer of the semiconductor–electrolyte interface, respectively [37]. According to the fitting results from the Nyquist plots using the proposed circuit models, the R_{CT} is approximately 6,510, 2,594, 3,566, and 12,665 Ω for the pristine ZnO, ZS-1, ZS-2, and ZS-3 respectively. The smaller R_{CT} of ZS-1 is ascribed to a faster charge transfer and higher separation rate of photogenerated electron–hole pairs in the composite structure [34], which supports the aforementioned photoresponse performance of the samples. Similarly, in ZnS or $ZnIn_2S_4$-modified ZnO nanorods, the decoration of suitable sulfides substantially decreases the R_{CT} of the ZnO–sulfides system, and therefore, obtains an enhanced photoresponse in comparison with the pristine ZnO nanorods [38]

Figure 9(a) shows the Mott–Schottky (M–S) plots of the pristine ZnO template. The positive slope in the M–S plots indicates the n-type nature of ZnO [27]. Moreover, the flat band potential at the electrolyte/electrode interface can be estimated from the M–S curves according to the M–S equation [34]. By extrapolating the *X*-axis intercepts of the linear region in the M–S curve, the flat band potential of ZnO has been determined to be approximately −0.5 eV (*vs* NHE). The evaluated value is close to the hydrothermally derived ZnO nanorods that have a flat band potential of −0.55 V (*vs* NHE) [39]. Compared with the flat band potential of the ZnO template, the value of the representative ZnO–ZnS heterogeneous structure (ZS-1) was more negative in Figure 9(b). The flat band potential of ZS-1 is estimated to be −0.63 eV. A more negative flat band reflects a smaller barrier to the charge transfer and can induce more electrons accumulation in the conduction band of the sample, thus suppressing the recombination of photogenerated electron–hole pairs [40]. A negative shift of the flat band level of the ZnO–ZnS composite in comparison with that of the ZnO template means a lifted Fermi level after vulcanization of the ZnO

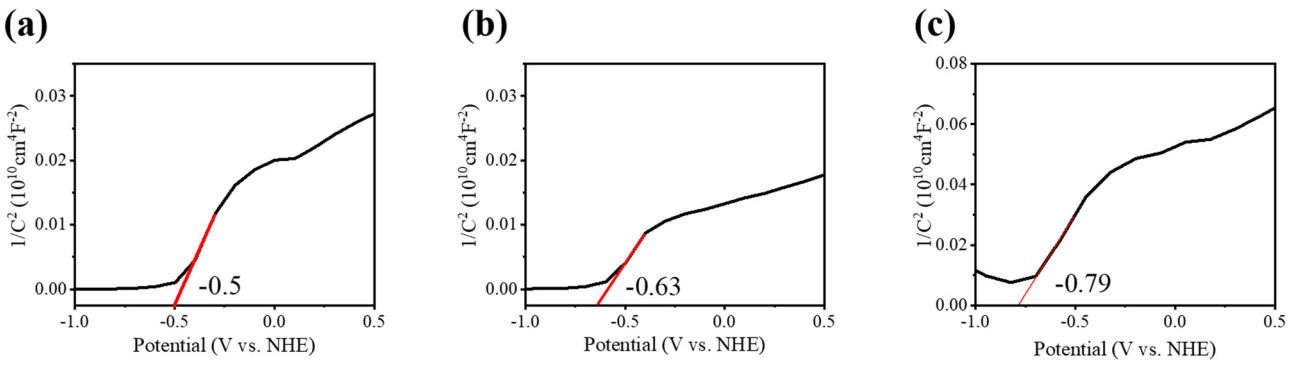

Figure 9: Mott–Schottky plots of various products: (a) ZnO, (b) ZS-1, and (c) ZnS.

sheet template, and the more negative flat band potential of the ZnO sheet template after vulcanized modification means an enlarged degree of band bending in the material system [38]. Similarly, the M–S result of the g-C_3N_4-modified TiO_2 heterostructure also exhibits the more negative flat band potential in the heterostructure with respect to that of the TiO_2 template, and an enhanced charge separation efficiency is demonstrated in the g-C_3N_4-modified TiO_2 heterostructure [41]. Furthermore, it has been shown that the conduction band energy (E_{CB}) for the n-type semiconductor is more negative, *i.e.*, about 0.1 eV than its flat band potential. [42]; therefore, the E_{CB} of the pristine ZnO template herein can be evaluated as −0.6 eV *vs* NHE. Notably, for the construction of the ZnO/ZnS heterogeneous band structure for the ZS-1, the referenced M–S plot of a single ZnS phase is displayed in Figure 9(c), and the E_{CB} of the ZnS is found to be roughly up to −0.89 eV *vs* NHE. Combined with the band gap energy obtained from the previous UV-vis results, the valence band energies (E_{VB}) for the ZnO and ZnS are calculated to be 2.6 eV and 2.51 eV *vs* NHE, respectively, according to the equation $E_{VB} = E_{CB} + E_g$.

Figure 10(a) presents the impressed potential-dependent degradation efficiency of the RhB solution by ZS-1 under 30 min irradiation. The PEC-degradation level of the RhB solution increased with increasing the impressed potential from 0 V to 0.5 V, and PEC-degradation efficiency of RhB solution reached a peak value of 58% at 0.5 V. Once the impressed potential exceeded 0.5 V, the degradation rate decreased (54%; 0.75 V). The result of Figure 10(a) demonstrates that a higher impressed potential (larger than 0.5 V) might result in reallocation of the space charge layers, further hindering the degradation efficiency [43]. Moreover, the ZS-1 was difficult to efficiently separate the photoinduced charges if the impressed voltage was lower than 0.5 V. Therefore, the optimal impressed potential for the ZnO–ZnS composite to the PEC-degrade RhB solution was chosen to be 0.5 V in this study. The photoelectrocatalytic performance of the ZnO template and various ZnO/ZnS composites toward the RhB solution is shown in Figure 10(b)–(e). The absorbance spectra intensity of the aqueous RhB solution decreased with irradiation duration for all the photoelectrocatalysts. In the PEC-degradation system, the absorbance peak of the RhB solution decreased during degradation without blue shift indicating the destruction of C═N, C═C, and C═O of the dye molecules due to the enhanced catalytic activity, and the final degradation products might consist of low-molecular-weight organic, CO_2, H_2O, *etc.* [43]. Figure 10(f) shows the RhB degradation efficiencies of ZnO, ZS-1, ZS-2, and ZS-3 are 57, 82, 72, and 43% under 60 min irradiation, respectively. Comparatively, the ZS-1 shows the highest degradation level toward the RhB solution among various control samples at the same given test convictions. Figure 10(g) presents the kinetic behaviors of the RhB solution degraded by ZnO and various ZnO–ZnS composites; the degradation rates of the RhB solution follow the pseudo-first-order reaction according to the simplified Langmuir–Hinshelwood model, $-\ln(C_t/C_0) = kt$, where C_0 is the initial concentration of the RhB solution, C_t is the concentration of that at different intervals during the degradation process, and k is the reaction rate constant (min^{-1}) [44]. The evaluated PEC-degradation rate constant of ZS-1 is 0.02493 min^{-1}, which is 1.8, 1.2, and 2.8 times that of ZnO, ZS-2, and ZS-3, respectively. The PEC-degradation performance of ZS-1 and ZS-2 towards RhB solution is superior to that of the ZnO template, revealing the construction of ZnO–ZnS composite structure with suitable vulcanization conditions is beneficial to improve the PEC-degradation activity of the ZnO template. Furthermore, the recycling tests are conducted for the ZS-1 five times (Figure 10(h)). Notably, after five cycles, only a slight decrease of the

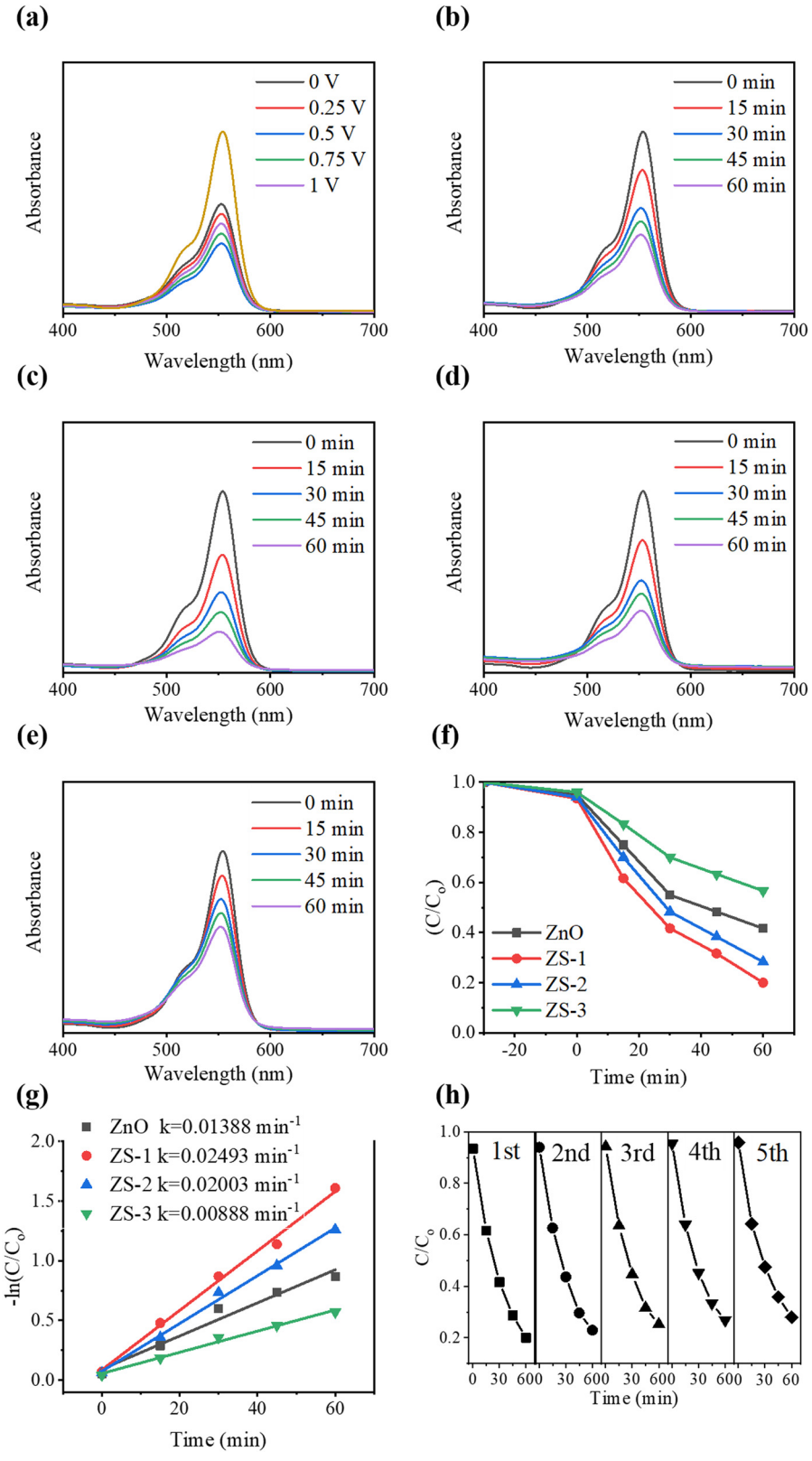

Figure 10: (a) Absorbance spectra intensity variation of the RhB solution under different impressed voltages with the ZS-1. Absorbance spectra intensity variation of the RhB solution as a function of irradiation time with various products as photoelectrocatalysts: (b) ZnO, (c) ZS-1, (d) ZS-2, and (e) ZS-3. (f) C/C_0 *vs* irradiation time plot. (g) The reaction rate constants of various products. (h) Recycling PEC-degradation tests of the ZS-1 toward RhB solution.

photoelectrocatalytic activity is found, and 73% of RhB is degraded. The ZS-1 still maintains good photocatalyst activity (>70%) for RhB dye degradation herein, inferring that the prepared ZS-1 porous composite sheet catalyst is effective and reusable under sunlight irradiation.

Based on the experimental results, the possible photogenerated electron–hole pair transfer steps inside the ZnO/ZnS photoanode, and the degradation mechanism toward RhB dyes is shown in Figure 11(a). In the ZnO/ZnS composite system, the CB position of ZnO was located at −0.6 eV and that of ZnS was located approximately −0.89 eV from the M–S results. Figure 11(a) indicates that the constructed ZnO/ZnS system exhibited a staggered type-II band alignment configuration, which can lead to a spatial separation of the photoinduced electrons and holes. Notably, the oxidation ($\cdot O_2^-/O_2$,) and reduction ($\cdot OH/H_2O$) potentials were −0.33 and +2.27 eV (*vs* NHE), respectively [2]. Excitation of electrons will take place in ZnO and ZnS simultaneously under irradiation. As the CB of ZnO is at a lower energy level than ZnS, the photogenerated electron will be transferred from CB of ZnS to the CB of ZnO, and further transported to the Pt counter electrode under an applied potential. By contrast, holes will migrate from the valence band (VB) of ZnO to the VB of ZnS, leading to the improved separation efficiency of photogenerated electron–hole pairs under the PEC system. The electrons at the Pt electrode and holes at the VB of ZnS would subsequently react with oxygen and water, respectively, to produce active superoxide and hydroxyl radicals for degradation processes. For further understanding of the photoelectrocatalytic mechanism, it is important to investigate the active species formed during the photoelectrocatalytic process toward the RhB solution. Benzoquinone (BQ), edentate disodium (EDTA), and *tert*-butyl alcohol (*t*-BuOH) were employed to scavenge the superoxide radicals ($\cdot O_2^-$), the hole (h^+), and hydroxyl radicals ($\cdot OH$), respectively, herein. As shown in Figure 11(b), the photoelectrocatalytic activity of ZS-1 has been significantly decreased when BQ is added, indicating the superoxide radicals ($\cdot O_2^-$) are the main reactive species in the photodegradation process. Comparatively, when introducing EDTA and *t*-BuOH, the degradation has been decreased for a lower degree, suggesting that h^+ and $\cdot OH$ also participate in the photocatalytic reaction for the ZS-1 toward RhB solution, but the effect is smaller than that of the $\cdot O_2^-$ species. Based on the above results, a schematic diagram of the possible degradation mechanisms of the photoinduced charges in the ZS-1 heterostructure is also constructed in Figure 11(a). The type II alignment of the ZnO–ZnS junction promoted the electron flowing from CB_{ZnS} to CB_{ZnO} and further transport to the Pt counter electrode, and then the O_2 accepted the electrons to generate $\cdot O_2^-$. Furthermore, VB_{ZnS} (2.51 eV) was more positive than the highest unoccupied molecular orbital (HOMO) of RhB (1.6 eV), the holes at the VB of ZnS can directly degrade RhB molecules and/or reaction with H_2O molecules for $\cdot OH$ radicals to degrade RhB molecules. Similarly, because of a more positive potential than the HOMO of RhB, photoinduced holes at the VB of Bi_2WO_6 in WO_3/Bi_2WO_6 heterostructures can directly react with RhB molecules or react with H_2O to generate $\cdot OH$ radicals to degrade RhB dyes effectively. [45]. As the applied potential accelerates the separation and transfer efficiency of photoinduced charges, it results in high PEC degradation efficiency of ZS-1. We put forward the possible action trails for reactive species as follows:

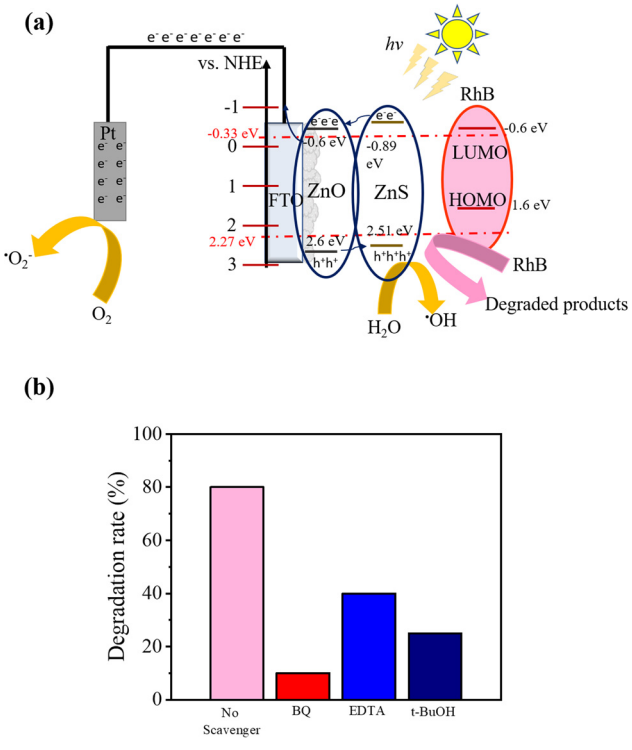

Figure 11: (a) The possible band structures and PEC-degradation mechanism of the ZS-1 toward RhB solution. (b) Scavenger tests of the RhB solution containing ZS-1.

$$ZnO + h\nu \rightarrow ZnO(e^- + h^+), \quad (1)$$

$$ZnS + h\nu \rightarrow ZnS(e^- + h^+), \quad (2)$$

$$e^-(Pt) + O_2 \rightarrow \cdot O_2^-, \quad (3)$$

$$h^+(VB_{ZnS}) + H_2O \rightarrow \cdot OH + H^+, \quad (4)$$

$$\cdot O_2^-, h^+, \cdot OH + RhB \rightarrow CO_2 + H_2O. \quad (5)$$

The aforementioned potential enhanced photoinduced charge separation is similar to the PEC-degradation of In_2O_3–ZnO composites with a type II band alignment toward the MB solution [46]. The electron drift and hole capture in Type II band alignment will suppress the recombination of photoinduced electron–hole pairs. Meanwhile, the applied voltage will rapidly prompt the photogenerated electrons to move to the external circuit rapidly, which tremendously reduces the recombination of electron–hole pairs. The improved photoelectrocatalytic activity of ZS-1 and ZS-2 composites with suitable ZnS/ZnO phase ratios than that of the pristine ZnO template herein was mainly ascribed to the formation of heterojunctions, which improved the absorption efficiency of light and inhibited the recombination of the photogenerated electron–hole pairs and the apparent synergetic effect between photo- and electrocatalysis, which facilitated charge generation, separation, and transfer. It has been shown that the comparative component ratio in the heterostructures is highly associated with their photocatalytic performances [46]. Moreover, the porous structure of the composites because of the high specific surface area is also beneficial to the photocatalytic activity [47]. Based on the aforementioned points, the porous structure and the optimal ZnS/ZnO phase ratio in the ZS-1 sheet impacted the superior photoelectrocatalytic performance toward degrading RhB dyes with respect to other ZnO–ZnS composites in this study. Similar porous structure and composition ratio effects dominating the optimal photocatalytic activity have also been demonstrated in ZnS–SnS_2 porous nanosheets [47].

4 Conclusion

The sheet-like ZnO–ZnS composites were successfully synthesized by the hydrothermal vulcanization method of porous ZnO sheet templates. The microstructure and composition analyses results reveal that the sulfur precursor concentration affected the ZnO/ZnS phase ratio and surface morphology of the as-synthesized ZnO–ZnS sheet composites. Compared with pristine ZnO, the ZnO–ZnS composites with the S/O atomic composition ratios of 0.61 and 0.85 substantially reduced the recombination rate of photogenerated electron–hole pairs by enhanced charge separation. By contrast, the ZnO–ZnS composite with the higher S/O atomic composition ratio of 3.63 decreased the photoactivity. The suitable ZnO/ZnS phase ratio and the porous surface feature made the ZS-1 porous sheet composite exhibit superior photoactivity among various control samples. In this study, the ZS-1 photoanode had a high photocurrent density of 1.22 mA/cm^2 at 0.5 V (*vs* Ag/AgCl), and highly efficient PEC-degradation ability toward RhB solution to over 80% at 0.5 V. The integration of the hydrothermally derived porous ZnO sheet template with a vulcanization process to control surface porous features and the ZnO/ZnS phase ratio by varying sulfur precursor concentrations is a promising approach to design the ZnS–ZnO sheet composite with various degrees of photoactive performances for photoelectrocatalyst applications.

Funding information: This research was funded by the Ministry of Science and Technology of Taiwan, Grant No. MOST 108-2221-E-019-034-MY3.

Author contributions: All authors have accepted responsibility for the entire content of this manuscript and approved its submission.

Conflict of interest: The authors state no conflict of interest.

References

[1] Das S, Srivastava V. An overview of the synthesis of CuO–ZnO nanocomposite for environmental and other applications. Nanotechnol Rev. 2018;7(3):267–82.
[2] Liang Y-C, Zhao W-C. Crystal growth and design of disk/filament ZnO-decorated 1D TiO_2 composite ceramics for photo-excited device applications. Nanomaterials. 2021;11(3):667–78.
[3] Dwivedi P, Jatrana I, Khan A, Khan A, Satiya H, Khan M, et al. Photoremediation of methylene blue by biosynthesized ZnO/Fe_3O_4 nanocomposites using Callistemon viminalis leaves aqueous extract: a comparative study. Nanotechnol Rev. 2021;10(1):1912–25.
[4] Hu J, Ding J, Ai J, Li H, Li S, Ma Q, et al. Room temperature growth of ZnO with highly active exposed facets for photocatalytic application. Nanotechnol Rev. 2021;10(1):919–32.
[5] Sardar S, Pal S. Ultrafast photoinduced carrier dynamics at ZnO nanohybrid interfaces for light-harvesting applications. Nanotechnol Rev. 2016;5(1):113–34.
[6] Liang Y-C, Deng X-S. Structure dependent luminescence evolution of c-axis-oriented ZnO nanofilms embedded with silver nanoparticles and clusters prepared by sputtering. J Alloy Compd. 2013;569(25):144–9.
[7] Laurenti M, Cauda V. Porous zinc oxide thin films: synthesis approaches and applications. Coatings. 2018;8(2):67–91.

[8] Lee G-J, Wu JJ. Recent developments in ZnS photocatalysts from synthesis to photocatalytic applications – a review. Powder Technol. 2017;318:8–22.
[9] Chen W, Ruan H, Hu Y, Li D, Chen Z, Xian J, et al. One-step preparation of hollow ZnO core/ZnS shell structures with enhanced photocatalytic properties. CrystEngComm. 2012;14(19):6295–305.
[10] Wang J, Guo P, Guo Q, Jönsson PG, Zhao Z. Fabrication of novel g-C_3N_4/nanocage ZnS composites with enhanced photocatalytic activities under visible light irradiation. CrystEngComm. 2014;16(21):4485–92.
[11] Lv P, Fu W, Yang H, Sun H, Chen Y, Ma J, et al. Simple synthesis method of Bi_2S_3/CdS quantum dots cosensitized TiO_2 nanotubes array with enhanced photoelectrochemical and photocatalytic activity. CrystEngComm. 2013;15(37):7548–55.
[12] Li S, Chen J, Hu S, Wang H, Jiang W, Chen X. Facile construction of novel Bi_2WO_6/Ta_3N_5 Z-scheme heterojunction nanofibers for efficient degradation of harmful pharmaceutical pollutants. Chem Eng J. 2020;402(15):126165.
[13] Oluwalana AE, Ajibade PA. Preparation and morphological studies of tin sulfide nanoparticles and use as efficient photocatalysts for the degradation of rhodamine B and phenol. Nanotechnol Rev. 2022;11(1):883–96.
[14] He K, Chen Y, Mei M. Study on influencing factors of photocatalytic performance of CdS/TiO_2 nanocomposite concrete. Nanotechnol Rev. 2020;9(1):1160–9.
[15] Gao X, Wang J, Yua J, Xu H. Novel ZnO–ZnS nanowire arrays with heterostructures and enhanced photocatalytic properties. CrystEngComm. 2015;17(33):6328–37.
[16] Liang Y-C, Li T-H. Controllable morphology of Bi_2S_3 nanostructures formed *via* hydrothermal vulcanization of Bi_2O_3 thin-film layer and their photoelectrocatalytic performances. Nanotechnol Rev. 2022;11(1):284–97.
[17] Chen X, Yang Z-T, Wang N, Gao X, Wang G, Song C, et al. Fabrication of Ag/ZnO hollow nanospheres and cubic TiO_2/ZnO heterojunction photocatalysts for RhB degradation. Nanotechnol Rev. 2021;10(1):1349–58.
[18] Li W, Wang G, Chen C, Liao J, Li Z. Enhanced visible light photocatalytic activity of ZnO nanowires doped with Mn^{2+} and Co^{2+} ions. Nanomaterials. 2017;7(1):20–31.
[19] Chen Y-C, Wang C-H, Lin H-Y, Li B-H, Chen W-T, Liu C-P. Growth of Ga-doped ZnS nanowires constructed by self-assembled hexagonal platelets with excellent photocatalytic properties. Nanotechnology. 2010;21(45):455604–12.
[20] Liang Y-C, Lo Y-R, Wang C-C, Xu N-C. Shell layer thickness-dependent photocatalytic activity of sputtering synthesized hexagonally structured ZnO–ZnS composite nanorods. Materials. 2018;11(1):87–97.
[21] Liang Y-C, Wang C-C. Surface crystal feature-dependent photoactivity of ZnO–ZnS composite rods *via* hydrothermal sulfidation. RSC Adv. 2018;8(9):5063–70.
[22] Li X, Li X, Zhu B, Wang J, Lan H, Chen X. Synthesis of porous ZnS, ZnO and ZnS/ZnO nanosheets and their photocatalytic properties. RSC Adv. 2017;7(49):30956–62.
[23] Lin D, Wu H, Zhang R, Zhang W, Pan W. Facile synthesis of heterostructured ZnO–ZnS nanocables and enhanced photocatalytic activity. J Am Ceram Soc. 2010;93(10):3384–9.
[24] Athauda TJ, Madduma-Bandarage USK, Vasquez Y. Integration of ZnO/ZnS nanostructured materials into a cotton fabric platform. RSC Adv. 2014;4(106):61327–32.
[25] Liang Y-C, Xu N-C. Synthesis of TiO_2–ZnS nanocomposites *via* sacrificial template sulfidation and their ethanol gas-sensing performance. RSC Adv. 2018;8(40):22437–46.
[26] Liang Y-C, Liu S-L. Structure-dependent gas detection ability of clustered ZnS crystallites with heterostructure and tube-like architecture. Acta Materialia. 2015;88(15):245–51.
[27] Liang Y-C, Hung C-S, Zhao W-C. Thermal annealing induced controllable porosity and photoactive performance of 2D ZnO sheets. Nanomaterials. 2020;10(7):1352.
[28] Liang Y-C, Chang C-W. Improvement of ethanol gas-sensing responses of ZnO–WO_3 composite nanorods through annealing induced local phase transformation. Nanomaterials. 2019;9(5):669.
[29] Ranjith KS, Senthamizhan A, Balusamy B, Uyar T. Surface nanograined shell wall controlled ZnO–ZnS core-shell nanofibers: shell wall thickness dependent visible photocatalytic properties. Catal Sci Technol. 2017;7(5):1167–80.
[30] Liang Y-C, Lo Y-J. High-temperature solid-state reaction induced structure modifications and associated photoactivity and gas-sensing performance of binary oxide one-dimensional composite system. RSC Adv. 2017;7(47):29428–39.
[31] Kate R, Khore S, Chauhan R, Kawade U, Naik S, Kale B, et al. Solid state low temperature synthesis approach for ZnO–ZnS nanoheterostructure with functionality as a photocatalyst for H_2 production and for DSSC. J Alloy Compd. 2021;858(25):158348.
[32] Jabeen U, Shah SM, Ullah Khan S. Photocatalytic degradation of Alizarin red S using ZnS and cadmium doped ZnS nanoparticles under unfiltered sunlight. Surf Interfaces. 2017;6:40–9.
[33] Kim H, Yang BL. A polyaniline-coated ZnS/ZnO/FTO photoelectrode for improving photocorrosion prevention and visible light absorption. N J Chem. 2019;43(42):16699–6705.
[34] Liang Y-C, Zhao W-C. Morphology-dependent photocatalytic and gas-sensing functions of three-dimensional TiO_2–ZnO nanoarchitectures. CrystEngComm. 2020;22(44):7575–89.
[35] Liang Y-C, Chiang K-J. Coverage layer phase composition-dependent photoactivity of one-dimensional TiO_2–Bi_2O_3 composites. Nanomaterials. 2020;10(5):1005.
[36] Liang Y-C, Chiang K-J. . Design and tuning functionality of rod-like titanium dioxide–nickel oxide composites *via* a combinational methodology. Nanotechnology. 2020;31(19):195709.
[37] Li C, Chen S, Wang Y, Hou Z. ZnO/ZnS heterostructures grown on Zn foil substrate by hydrothermal method for photoelectrochemical water splitting. Int J Hydrog Energy. 2019;44(47–4):25416–27.
[38] Wei C, Gu X, Li K, Song J, Zhao Y, Qiang Y. Enhanced photoelectrochemical activities of ZnO nanorod arrays after a modification of ZnS or $ZnIn_2S_4$. J Electron Mater. 2019;48:7345–51.
[39] Majumder T, Hmar JJL, Debnath K, Gogurla N, Roy JN, Ray SK, et al. Photoelectrochemical and photosensing behaviors of hydrothermally grown ZnO nanorods. J Appl Phys. 2014;116:034311.
[40] Li Z, Chen Y, Shen J, Cui X. Facile synthesis of heterogeneous Li_2TiO_3/TiO_2 nanocomposite with enhanced photoelectrochemical water splitting. N J Chem. 2017;41(14):6305–14.
[41] Wang H, Liang Y, Liu L, Hu J, Cui W. Highly ordered TiO_2 nanotube arrays wrapped with g-C_3N_4 nanoparticles for efficient charge separation and increased photoelectrocatalytic degradation of phenol. J Hazard Mater. 2018;344(15):369–80.

[42] Hao X, Wang Y, Zhou J, Cui Z, Wang Y, Zou Z. Zinc vacancy-promoted photocatalytic activity and photostability of ZnS for efficient visible-light-driven hydrogen evolution. Appl Catal B: Environ. 2018;221:302–11.
[43] Wang Y, Lu N, Luo M, Fan L, Zhao K, Qu J, et al. Enhancement mechanism of fiddlehead-shaped TiO_2-$BiVO_4$ type II heterojunction in SPEC towards RhB degradation and detoxification. Appl Surf Sci. 2019;463(1):234–43.
[44] Liang Y-C, Xu N-C, Chiang K-J. Surface morphology-dependent functionality of titanium dioxide–nickel oxide nanocomposite semiconductors. Nanomaterials. 2019;9(12):1651.
[45] Peng Y, Chen Q-G, Wang D, Zhou H-Y, Xu A-W. Synthesis of one-dimensional WO_3–Bi_2WO_6 heterojunctions with enhanced photocatalytic activity. CrystEngComm. 2015;17(3):569–76.
[46] Zhao J, Ge S, Pan D, Pan Y, Murugadoss V, Li R, et al. Microwave hydrothermal synthesis of In_2O_3–ZnO nanocomposites and their enhanced photoelectrochemical properties. J Electrochem Soc. 2019;166(5):3074–83.
[47] Wang L, Jin G, Shi Y, Zhang H, Xie H, Yang B, et al. Co-catalyst-free ZnS-SnS_2 porous nanosheets for clean and recyclable photocatalytic H_2 generation. J Alloy Compd. 2018;753(15):60–7.